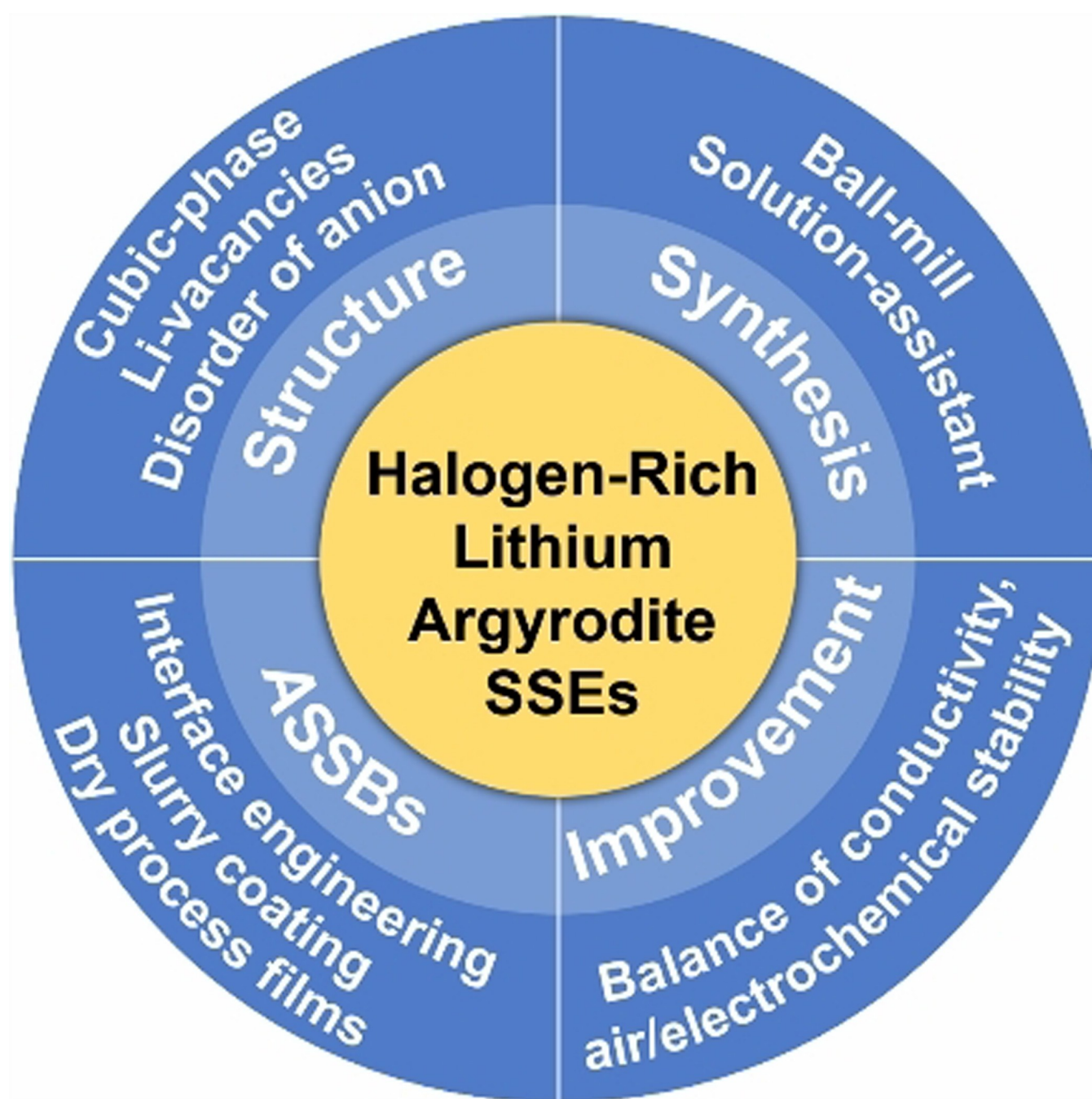Special
Collection

Halogen-Rich Lithium Argyrodite Solid-State Electrolytes: A Review

Linfeng Peng,[a] Chuang Yu,*[a] Shijie Cheng,[a] and Jia Xie*[a]

Exploring solid electrolytes (SEs) with high ionic conductivity, excellent chemical/electrochemical stability, and excellent compatibility with electrodes is important for promoting the development of all-solid-state batteries (ASSBs). Halogen-rich lithium argyrodite electrolytes have received a lot of attention recently due to their ultrahigh room-temperature lithium-ion conductivity and relatively low cost. In this review, the properties of the halogen-rich argyrodite electrolytes are presented in terms of their crystal structure, ionic conduction mechanism, and compatibilities with oxide cathode and Li-metal anode. Secondly, the preparation process of SE film and the performances of ASSBs based on this electrolyte are summarized. Finally, the challenges and the next research directions of the electrolytes are proposed. Halogen-rich lithium argyrodite electrolytes are one of the promising sulfide electrolytes, the collation of this paper can provide us with a better understanding of the current development status of this type of electrolyte and advance their further development.

1. Introduction

The all-solid-state battery (ASSB) is a prominent technology for next-generation energy storage devices because of its high energy density and extraordinary safety.[1–13] As an essential component of ASSBs, the solid electrolytes (SEs) have a direct impact on the performance of ASSBs. High-performance SEs require high ionic conductivity, low interfacial impedance, chemical/electrochemical and thermal stability, high mechanical strength, and good processability.[5,6,14,15] Reported SEs include oxides, sulfides, halides, and polymers.[16] The properties of different SEs vary considerably, and each has its pros and cons. Oxide electrolytes show superior redox stability and air stability, while their grain boundary impedance is high. Therefore, high-temperature heat treatment around 1000 °C is required to reduce the grain boundary impedance for high ionic conductivity.[17–19] Sulfide electrolytes have high lithium-ion conductivity ($\sim 10^{-2}$ S cm^{-1}) and low interfacial impedance.[20–26] However, the poor air stability and narrow electrochemical stability window hinder their practical application.[2,4,6–8,27–29] Halide electrolytes exhibit excellent compatibility with oxide cathodes, but their poor electrochemical stability with lithium metal and high hygroscopicity prevent their wide application in ASSBs.[16,30,31] Polymer electrolytes have good flexibility and processability, while their ionic conductivities are low ($< 10^{-4}$ S cm^{-1}), and their thermal stabilities are inferior.[32,33]

Sulfide electrolytes have received widespread attention in industry and academia in recent years since the report of Li$_{10}$GeP$_2$S$_{12}$ (LGPS) in 2011.[22] LGPS with ionic conductivity comparable to liquid electrolytes, which stimulates the interest for its study. However, the high cost of Ge's raw material and the instability of lithium metal limit its practical application. In contrast, lithium argyrodite electrolytes (Li$_{7.0-y}$PS$_{6.0-y}$X$_y$, $y = 0$–

2.0) can be synthesized by low-cost LiX (X = Cl, Br, I), having a major advantage over LGPS in terms of manufacturing cost. More importantly, with the development of the last few years, the ionic conductivity of halogen-rich lithium argyrodites (Li$_{7.0-y}$PS$_{6.0-y}$X$_y$, $y > 1.0$) reaches the level of liquid electrolyte ($> 10^{-2}$ S cm^{-1}) and even exceeds that of LGPS.[24,34–40] Furthermore, Li$_{5.5}$PS$_{4.5}$Cl$_{1.5}$ (LPSC-1.5) has demonstrated electrochemical stability and good mechanical properties. The key properties of common sulfide electrolytes have been listed in Table 1.[41] Recently, several reports have demonstrated the effect of halogen content on the ionic conductivity, electrochemical stability, and air stability of lithium argyrodite electrolytes.[37,38,42–45] The halogen-rich argyrodite electrolytes (Li$_{7.0-y}$PS$_{6.0-y}$X$_y$, $y > 1.0$) tend to exhibit greater potential than the halogen-poor ones (Li$_{7.0-y}$PS$_{6.0-y}$X$_y$, $y \leq 1.0$). A generalization of halogen-rich argyrodite electrolytes will help us better understand their performance and developmental status as well as promote their application in ASSBs. However, most of the published reviews on lithium argyrodite electrolytes are about the entire development history and current status of this kind of electrolyte, and the description of halogen-rich argyrodite electrolytes is incomplete and does not highlight the importance of the class of electrolytes.[20,21,24]

In this review, we introduce the crystal structure and ionic conduction mechanism of halogen-rich lithium argyrodite electrolytes and first explain the origin of their high ionic conductivity. Second, we summarize the preparation methods of these electrolytes and introduce strategies for improving ionic conductivity, air stability, and electrochemical stability. Third, we systematically outline their application in all-solid-state batteries, including the real stability of the electrode/electrolyte interface and corresponding improvements. Several constructing processes for ASSBs are also introduced. Finally, present challenges and future outlooks are also presented.

[a] Dr. L. Peng, Prof. C. Yu, Prof. S. Cheng, Prof. J. Xie
State Key Laboratory of Advanced Electromagnetic Engineering and Technology
School of Electrical and Electronic Engineering
Huazhong University of Science and Technology
Wuhan 430074 (China)
E-mail: xiejia@hust.edu.cn
cyu2020@hust.edu.cn

2. Crystal structure & ion conduction mechanism

Lithium argyrodite electrolytes Li$_6$PS$_5$X (X = Cl, Br, I) with cubic crystal structures (F$\overline{4}3$m), which are composed of PS$_4^{3-}$ tetrahedra.[46–50] The S^{2-} and X$^-$ anions are disordered on the 4a and 4d (4c) sites in the lattice, while the Li$^+$ ion sites form cage-like polyhedra around them. The results of molecular dynamics

Batteries & Supercaps

Review
doi.org/10.1002/batt.202200553

Chemistry Europe
European Chemical
Societies Publishing

(MD) simulations indicate that the lithium ions jump through three paths in the cage-like polyhedron: "doublet" jumps ($48h$–$24g$–$48h$), intra-cage jumps ($48h$–$48h$), and inter-cage jumps. Halogen-rich argyrodites, $Li_{6-x}PS_{5-x}$ (Cl, Br, I)$_{1+x}$ ($0 \leq x \leq 1.0$), derive from substitution of S^{2-} with more X^- ($X = Cl$, Br, I). In general, the greater amount of halogen ions in the halogen-rich argyrodite structure, the more enhanced S/Cl disorder degree and more vacancies on the Li sites than Li_6PS_5X. Both resulted in improved ionic conductivity. In 2019, Nazar's group[39] synthesized a series of chlorine-rich argyrodite electrolytes $Li_{6-x}PS_5Cl_{1+x}$ ($x = 0$–0.6). The structure of LPSC-1.5 was confirmed through time-of-flight (TOF) neutron powder diffraction. The ionic conductivities of a series of compositions were measured by a combination of electrical impedance spectroscopy (EIS) and pulsed-field gradient (PFG) NMR. The crystal structure of LPSC-1.5 and the different occupancies (SOF) on the $4a$ and $4d$ ($4c$) sites between Li_6PS_5Cl (LPSC-1.0) and LPSC-1.5 are shown in Figure 1(a). The Li occupancy on the $48h$ site obtained from neutron diffraction data verifies more Li vacancies existed in LPSC-1.5 than that of LPSC-1.0, and so do the amount of Cl on both $4a$ and $4d$ ($4c$) sites. Gautam et al. calculated the distribution percentage and occupancies of Cl^- at both sites (Figure 1b).[35] The Cl^- occupancies of both sites increase as the Cl^- content increases, which changes the average charge on the two sites because of the charge difference between Cl^- and S^{2-} (Figure 1c).

Furthermore, the authors analyzed Li-ion migration pathways in argyrodite structures with different chlorine content by the bond valence sum method (Figure 1d, T2 and T5 represent different Li-ion sites). As shown in Figure 1(e), the T2-T2 jump exhibits the largest migration barrier, indicating that it is the rate-limiting step. The calculated T2-T2 migration barriers decrease with the increase in Cl content, suggesting a higher ionic conductivity, which is consistent with the results of the experimental activation energy (Figure 1f). However, in the synthesis process, there is a maximum solubility of Cl in the argyrodite structure. Beyond that, impurities or structural

changes start to be detected and the ionic conductivity decreases with additional chlorine content. Synthetic conditions also have an effect on the solubility of Cl in the structure. Adeli et al.,[39] Gautam et al.,[35] and Peng et al.[43] confirmed that the composition LPSC-1.5 exhibits the highest conductivity in the category $Li_{6-x}PS_{5-x}Cl_{1+x}$ ($0 \leq x \leq 1.0$), while Yu et al.[51] and Feng et al.[44] suggested $Li_{5.7}PS_{4.7}Cl_{1.3}$ (LPSC-1.3) and $Li_{5.3}PS_{4.3}Cl_{1.7}$ (LPSC-1.7) with the highest conductivity, respectively. The above difference in ionic conductivities mainly stems from the fact that sintering temperature and time affect the solubility of Cl in the structure. A similar rule of ionic conductivity is observed in the bromine-rich analogs.[38,52,53]

In conclusion, the crystal structure and ion conduction mechanism of the halogen-rich lithium argyrodites are similar to those of the conventional ones, the fast ion migration results from the increased S^{2-}/X^- anion mixing and more lithium vacancies in the structure.

3. Synthesis routes

A facile synthetic route is critical to driving the practical application of solid-state electrolytes. Commonly, the synthetic methods for halogen-rich lithium argyrodite electrolytes can be divided into solid- and liquid-phase ones. The solid-phase method yields samples with higher ionic conductivity, while the liquid-phase method is more suitable for large-scale production.

3.1. Solid-phase method

In 2021, Yu et al.[21] summarized three common solid-phase methods for preparing lithium argyrodite electrolytes: mechanical milling, mechanical milling followed by annealing, and direct solid-state sintering. Among these three synthesis routes, the first two involve a high-speed mechanical ball milling

Linfeng Peng received his MS degree from Wuhan Institute of Technology in 2016 and his PhD from Huazhong University of Science and Technology in 2022. Now, he is a postdoctoral researcher at Huazhong University of Science and Technology. His current research interest mainly focuses on solid electrolyte and solid-state battery.

Chuang Yu received his BS degree from Harbin Engineering University in 2009 and his PhD from Delft University of Technology in 2017. He joined Huazhong University of Science and Technology (HUST) as a Full Professor in 2020. His current research interests focus on solid electrolyte and solid-state battery. Email: cyu2020@hust.edu.c

Shijie Cheng received his Master and PhD in Electrical Engineering from the Huazhong University of Science (HUST) and Technology and the University of Calgary in 1981 and 1986, respectively. He is currently a member of Chinese Academy of Sciences and a full professor in the HUST. His research interests include power system control and stability analysis, energy storage and application of artificial intelligence in power systems.

Jia Xie received his BS degree from Peking University in 2002 and his PhD from Stanford University in 2008. He joined Huazhong University of Science and Technology (HUST) as a Full Professor in 2015. His current research interests focus on Power battery and the key materials, large-scale electrochemical energy storage technology for power grid and electric vehicle. Email: xiejia@hust.edu.cn

Batteries & Supercaps

Review
doi.org/10.1002/batt.202200553

Chemistry Europe
European Chemical
Societies Publishing

Table 1. Comparison of the key properties of common sulfide electrolytes.[41]

SE	σ_{rt} [mS/cm]	Electrochemical stability window by CV [V]	Young's modulus
LGPS	12.0 on sintering	0~7	Argyrodite > LGPS > Li$_3$PS$_4$ > Li$_7$P$_3$S$_{11}$
Argyrodite	24.0 on sintering (LPSB-1.7)[a]	0~10	
	9.4 on cold-press (LPSC-1.5)[b]		
Li$_7$P$_3$S$_{11}$	17.0 on sintering	0~5	
Li$_3$PS$_4$	0.16	0~5	

[a] Li$_{5.3}$PS$_{4.3}$Br$_{1.7}$; [b] Li$_{5.5}$PS$_{4.5}$Cl$_{1.5}$.
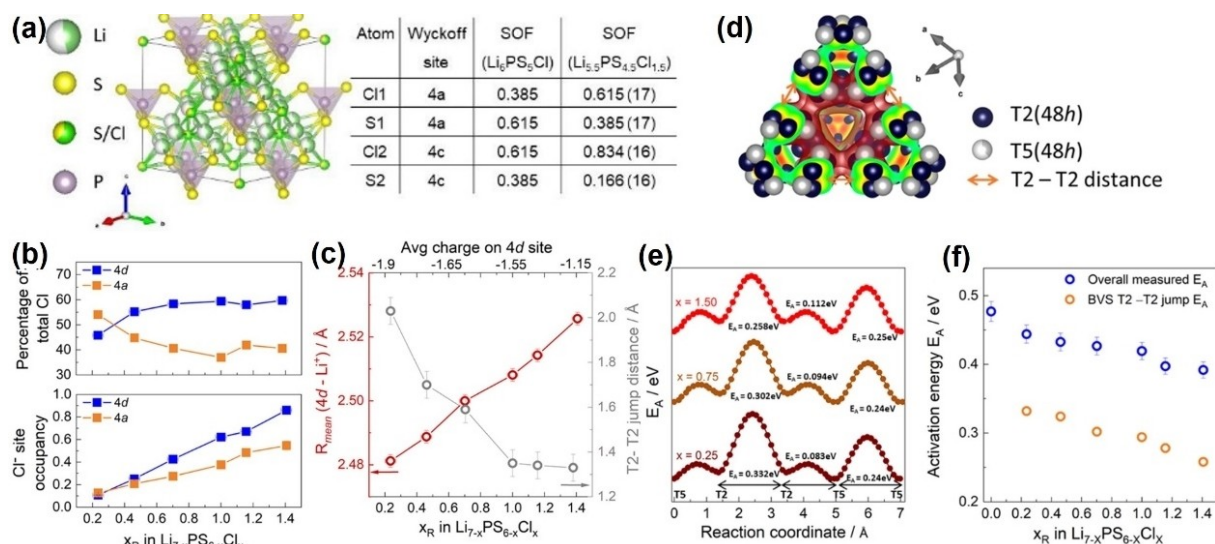
Figure 1. a) Crystal structure of Li$_{5.5}$PS$_{4.5}$Cl$_{1.5}$ showing the PS$_4^{3-}$ tetrahedra, the cage-like polyhedra formed by Li$^+$ ions, free S^{2-}/Cl$^-$ anions, and comparison of occupancies (SOF) on the 4a and 4c sites between Li$_6$PS$_5$Cl and Li$_{5.5}$PS$_{4.5}$Cl$_{1.5}$. Reproduced with permission from Ref. [39]. Copyright (2019) Wiley-VCH. b) Top panel shows the percentage of total Cl$^-$ content distributed across each of the two Wyckoff sites and the bottom panel shows the Cl$^-$ occupancy of the sites as it increases with increasing Cl$^-$ content. c) R_{mean}, representing the radial distance between the centers of the cage (Wyckoff 4d) and the mean Li$^+$ density of the surrounding cage, increases, and the T2-T2 distance (inter-cage jump) significantly decreases with increasing Cl$^-$ content. d) Li-ion migration pathways were analyzed using the bond valence sum method with additional chloride content, showing the T2-T2 jump distance, which represents the interconnected cages. e) Migration barrier along the T5-T2-T2-T5-T5 pathway that corresponds to transport from one cage to the next. f) Experimental activation energy, calculated T2-T2 migration barrier, that can be observed with additional chloride content. Reproduced with permission from Ref. [35]. Copyright (2021) American Chemical Society.

process, which causes the raw materials strongly adhesive to the balls and the inner wall of the jar which increases the difficulty in handling and leads to inconsistency of the products. On the contrary, the synthesis method of direct solid-state sintering avoids the above problem by not requiring a high-speed milling process and is therefore a suitable solid-phase synthesis method for preparing lithium argyrodite electrolytes on a large scale.

By using a straightforward solid-state sintering technique, we can modify the composition to produce chlorine-rich argyrodite electrolytes with high ionic conductivity (Figure 2a). Chlorine-rich lithium argyrodites Li$_{7-x}$PS$_{6-x}$Cl$_x$ ($x = 1.0$–2.0) were directly synthesized at an optimal annealing temperature of 500 °C for 15 h. Table 2 lists the ionic conductivities of Li$_{7-x}$PS$_{6-x}$Cl$_x$ ($x = 1.0$–2.0) at room temperature.[43] LPSC-1.5 is shown to be the optimized composition with remarkable ionic conductivity (9.03 mS/cm) at room temperature, which is even comparable to the existing liquid electrolyte. These conductivity values are significantly greater than those of samples prepared using a liquid-phase approach and are comparable to those of the argyrodite electrolytes obtained through complicated mechan-

Table 2. The detailed ionic conductivities of different halogen-rich lithium argyrodites.[43]

Li$_{7-x}$PS$_{6-x}$Cl$_x$	σ_{rt} [mS/cm]	E_a [eV]
$x = 1.0$	3.33	0.327
$x = 1.1$	4.00	0.325
$x = 1.2$	4.81	0.309
$x = 1.3$	5.37	0.305
$x = 1.4$	6.67	0.245
$x = 1.5$	9.03	0.271
$x = 1.6$	7.16	0.303
$x = 1.7$	2.15	0.230
$x = 1.8$	1.12	0.259
$x = 1.9$	0.114	0.336
$x = 2.0$	0.0107	0.277

ical milling followed by annealing.[39,54] The solubility of Cl in the structure is affected by synthetic variables like sintering time and temperature. Our XRD results show that the impurities start to appear in the structure of argyrodites Li$_{7-x}$PS$_{6-x}$Cl$_x$ ($x = 1.7$–2.0) when $x \geq 1.7$, causing a sharp decrease in ionic conductivity. Hu's group mixed the raw materials and calcined them to obtain a series of halogen-rich lithium argyrodite
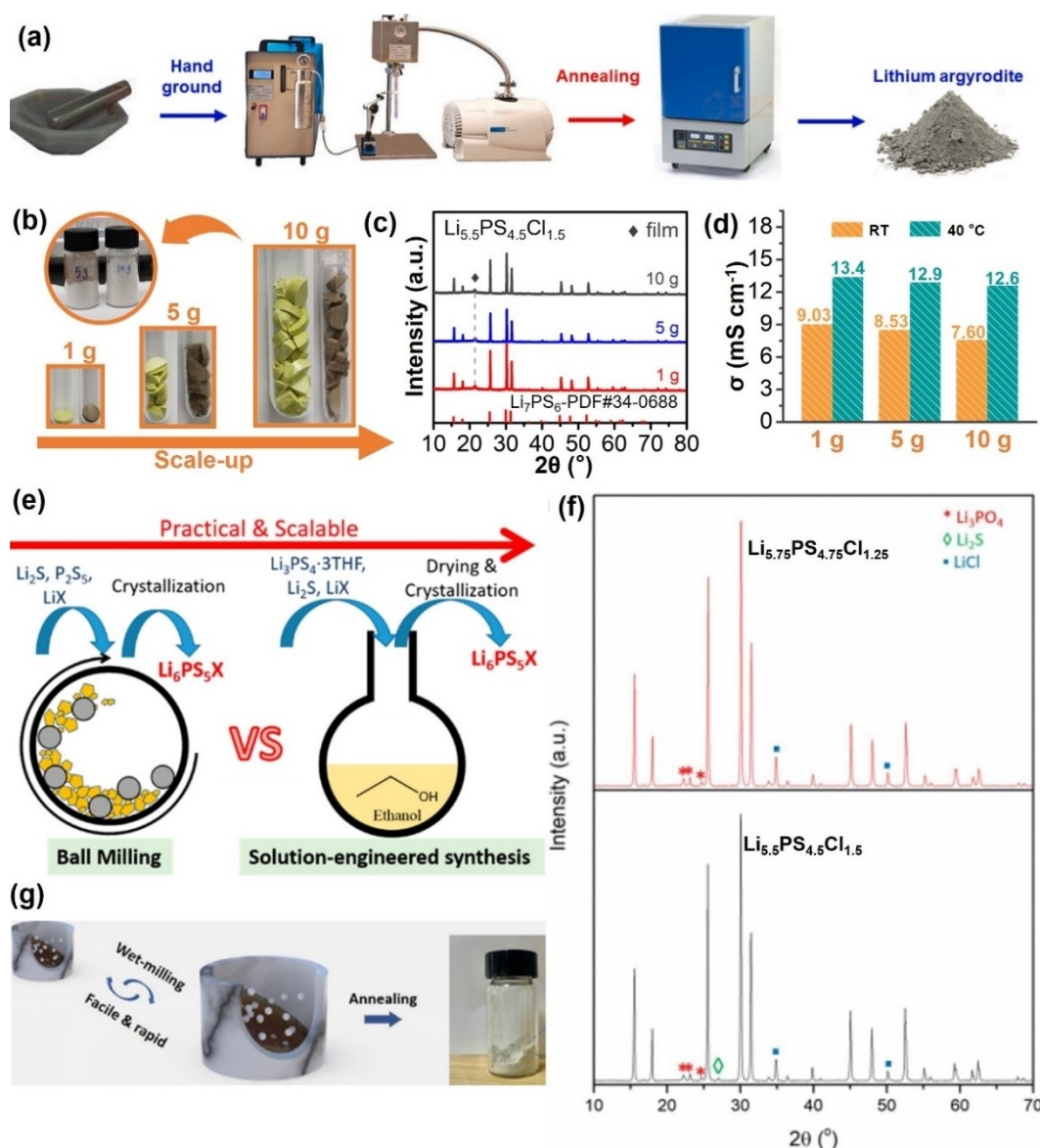
Batteries & Supercaps

Review
doi.org/10.1002/batt.202200553

Chemistry
Europe
European Chemical
Societies Publishing

Figure 2. a) Schematic of the solid-state sintering route for lithium argyrodite electrolytes. Reproduced with permission from Ref. [21]. Copyright (2021) Elsevier. b) The digital images of scale-up samples before and after sintering. c) XRD patterns and d) variation trend of the ionic conductivity of scale-up LPSC-1.5 samples at room temperature and 40 °C. Reproduced with permission from Ref. [43]. Copyright (2022) Elsevier. e) Schematic of ball milling and solution-engineered synthesis methods. f) XRD patterns of $Li_{5.75}PS_{4.75}Cl_{1.25}$ (red line) and LPSC-1.5 (black line). Reproduced with permission from Ref. [54]. Copyright (2019) American Chemical Society. g) Schematic of wet-milling synthesis of $Li_{6-x}PS_{5-x}Cl_{1+x}$ ($0 \leq x \leq 0.8$). Reproduced with permission from Ref. [55]. Copyright (2021) American Chemical Society.

electrolytes of $Li_{7-x}PS_{6-x}Cl_x$ and $Li_{7-x}PS_{6-x}Br_x$ ($x = 1.0$, 1.3, 1.5, 1.7, and 1.8).[38,44] The highest room temperature ionic conductivity of 17 and 24 mS/cm are observed in the sintered LPSC-1.7 and LPSB-1.7 pellets respectively. Liao et al.[53] synthesized bromine-rich argyrodite electrolytes $Li_{7-x}PS_{6-x}Br_x$ ($x = 1.0$–1.8) by first high-rotation milling the materials, then annealing them. $Li_{5.6}PS_{4.6}Br_{1.4}$ (LPSB-1.4) electrolyte delivers the highest conductivity of 6.91 mS/cm at ambient temperature. Electrolytes with various halogen contents attain the best ionic conductivities, due to modifications in synthetic parameters that impact the solubility of halogens in the argyrodite structure.

Furthermore, multiple amounts of LPSC-1.5 electrolytes (1, 5, and 10 g) per batch were produced to assess the viability of

scaling up the direct solid-state sintering process.[43] The samples that were acquired had comparable light dray colors (Figure 2b). The synthesis of LPSC-1.5 electrolyte can be carried out on a 10 g scale to produce pure lithium argyrodite phase and comparable ionic conductivity, according to XRD patterns and the results of ionic conductivities (Figure 2c and d). The LPSC-1.5 electrolytes' room-temperature conductivities gradually decrease as the amount of synthesis is increased. At a higher temperature (40 °C), however, the resulting electrolytes show negligible variations in lithium-ion conductivities. The equivalent conductivities for those electrolytes support this synthesis route's strong scalability (Figure 2d). These findings suggest that the straightforward solid-state reaction synthesis

Batteries & Supercaps

Review
doi.org/10.1002/batt.202200553

Chemistry
Europe
European Chemical
Societies Publishing

pathway for chlorine-rich lithium is a promising and scalable technique.

3.2. Liquid-phase method

The liquid-phase synthetic procedure of lithium argyrodite electrolytes often requires the inclusion of organic solvents, which has the advantage of facilitating homogenous mixing of the raw components and is more suited for batch production, as opposed to the solid-phase synthesis route.[55–61] But because organic solvents are frequently difficult to completely evaporate, the resulting electrolyte products often contain apparent impurities and have substantially poorer ionic conductivities than electrolytes made via a solid-phase approach.

$Li_{6-x}PS_{5-x}Cl_{1+x}$ ($x=0.25$ and 0.5) solid electrolytes with high Li-ion conductivities of up to 4 mS cm^{-1} at ambient temperature were obtained using a direct solution synthesis method in 2019, according to Zhou et al.[54] Tetrahydrofuran (THF) and ethanol were used to dissolve the $Li_3PS_4 \cdot 3THF$, Li_2S, and LiCl precursors (Figure 2e). The Li_3PS_4/solvent combination is created using THF as the solvent since it allows for a quicker reaction time (hours) than other solvents like dimethoxyethane (DME; 10 days) or acetonitrile (ACN; 2 days), as well as having a lower boiling point that makes removal easier. The totally combined reactants crystallized weakly after the solvents evaporated. To boost the level of crystallinity, the powder was next compressed into pellets and sintered at $550\,°C$ under a vacuum in a quartz tube covered with carbon. According to XRD patterns of the produced electrolytes, the major crystalline phase for the products is argyrodite (F-43 m), with minor amounts of Li_3PO_4, LiCl, and Li_2S impurities making up the remainder (Figure 2f).[54] Possible causes of the high impurity level include an interaction between PS_4^{3-} units and ethanol or a little amount of moisture in the ethanol. $Li_{5.75}PS_{4.75}Cl_{1.25}$ (LPSC-1.25) and LPSC-1.5 have calculated room temperature ionic conductivities of 3.0 and 3.9 mS cm^{-1}, respectively. The high conductivity values show that, because of their highly crystalline structures, the impurities in the solution-processed chlorine-rich argyrodite electrolytes do not considerably obstruct the Li^+ conduction. For solid electrolytes, the degree of crystallinity is a crucial consideration.

Wu et al. have investigated a simple method for synthesizing $Li_{6-x}PS_{5-x}Cl_{1+x}$ ($0 \leq x \leq 0.8$) chlorine-rich argyrodite electrolytes, in preparation for mass production (Figure 2g).[55] The precursor components were dispersed using anhydrous acetonitrile as the solvent. To remove the acetonitrile, the uniformly distributed precursor slurry was dried under a vacuum at $70\,°C$. Next, the precursor powder was preheated at a low temperature of $300\,°C$ for 1 hour, then it was once again annealed at $500\,°C$ for 4 hours. According to the electrolyte samples' XRD patterns, the highest Cl solubility in $Li_{6-x}PS_{5-x}Cl_{1+x}$ occurs at $x=0.7$. In the electrolytes with high Cl contents of $x=0.7$ and 0.8, the diffraction peaks of LiCl and other unidentified phases are clearly visible. As a result, the LPSC-1.6 pellet achieves the greatest ionic conductivity at an ambient temperature of 6.18 mS cm^{-1}. The reduction of the room temperature grain boundary impedance and the number of impurities in Cl-rich argyrodite electrolytes caused by the manipulation of the calcination temperature leads to high ionic conductivity.

4. Modification

By increasing the concentration of vacancies and creating more S^{2-}/X^- ($X=Cl$, Br, I) disorder in the structure, halogen-rich lithium argyrodite electrolytes can easily reach high ionic conductivities. However, for sulfide solid electrolytes, a promising ionic conductivity is not enough to advance their practical applications. Air stability and electrode compatibility are also necessary features. Doping can increase sulfide electrolyte's air stability and electrode compatibility, but it frequently causes the electrolyte's ionic conductivity to drop.[62–65]

The key to developing all-solid-sate batteries is learning how to modify sulfide electrolytes to equip them with high ionic conductivity, high air stability, and high electrode compatibility. Halogen-rich lithium argyrodite electrolytes with a high enough ionic conductivity allow us a lot of room to improve performance in other areas. The strategies for enhancing ionic conductivity, improving electrochemical stability, and air stability of halogen-rich lithium argyrodite electrolytes are described in detail below.

In 2020, Zhang et al.[66] reported that adding a little quantity of Al^{3+} to the Li^+ site increased the ionic conductivity of Li_6PS_5Br from 1.0 mS cm^{-1} to 2.4 mS cm^{-1} ($Li_{5.4}Al_{0.2}PS_5Br$). This improvement is relayed to shorter inter-cage jump distances, which are thought to be the step that determines the rate of ion migration. Inspired by these results, Adeli et al.[47] made an effort to raise the concentration of lithium vacancies by aliovalently doping the Li^+ site with Ca^{2+} in Cl-rich argyrodite electrolytes. The "super Cl-rich" substance $Li_{5.35}Ca_{0.1}PS_{4.5}Cl_{1.55}$ has an extraordinary diffusivity and a superionic room temperature conductivity of 10.2 mS cm^{-1} in the cold-pressed form. Additionally, as the Ca^{2+} level in Li sites grows, the structure's Cl^-/S^{2-} site disorder increases (Figure 3a). Taklu et al.[65] synthesized Cl-rich Li argyrodite $Li_{6+3x}P_{1-x}Cu_xS_{5-x}Cl_{1+x}$ ($x=0.1$, 0.2, 0.3, 0.4, and 0.5) using CuCl as a dual dopant. The Li argyrodite electrolytes with dual-doped Cl contents attain the highest ionic conductivity of 4.34 mS cm^{-1} and the lowest activation barrier of 0.25 eV at $x=0.1$. The higher charge carrier density (Li^+), and reduced electronegativity (EN) gap between brought on by chlorine are thought to work synergistically to explain the high ionic conductivity. In addition, the Vienna ab-initio simulation package (VASP) assessed the distance between 48 h Li ions for Li_6PS_5Cl and $Li_{6.3}P_{0.9}Cu_{0.1}S_{4.9}Cl_{1.1}$ samples (LPSC-1). For Li_6PS_5Cl and $Li_{6.3}P_{0.9}Cu_{0.1}S_{4.9}Cl_{1.1}$ the distance between two 48 h lithium ions in the Li_6S group is 3.298 and 2.997 Å, respectively (Figure 3b and c).

In the Li_6S group, the distance between two 48 h lithium ions must be reduced in order to create quick intra-cage leaps within the cage (48 h–48 h) and achieve lower activation energy than the pure Li_6PS_5Cl sample (LPSC-p). On the other hand, due to volume expansion, the distance between 48 h
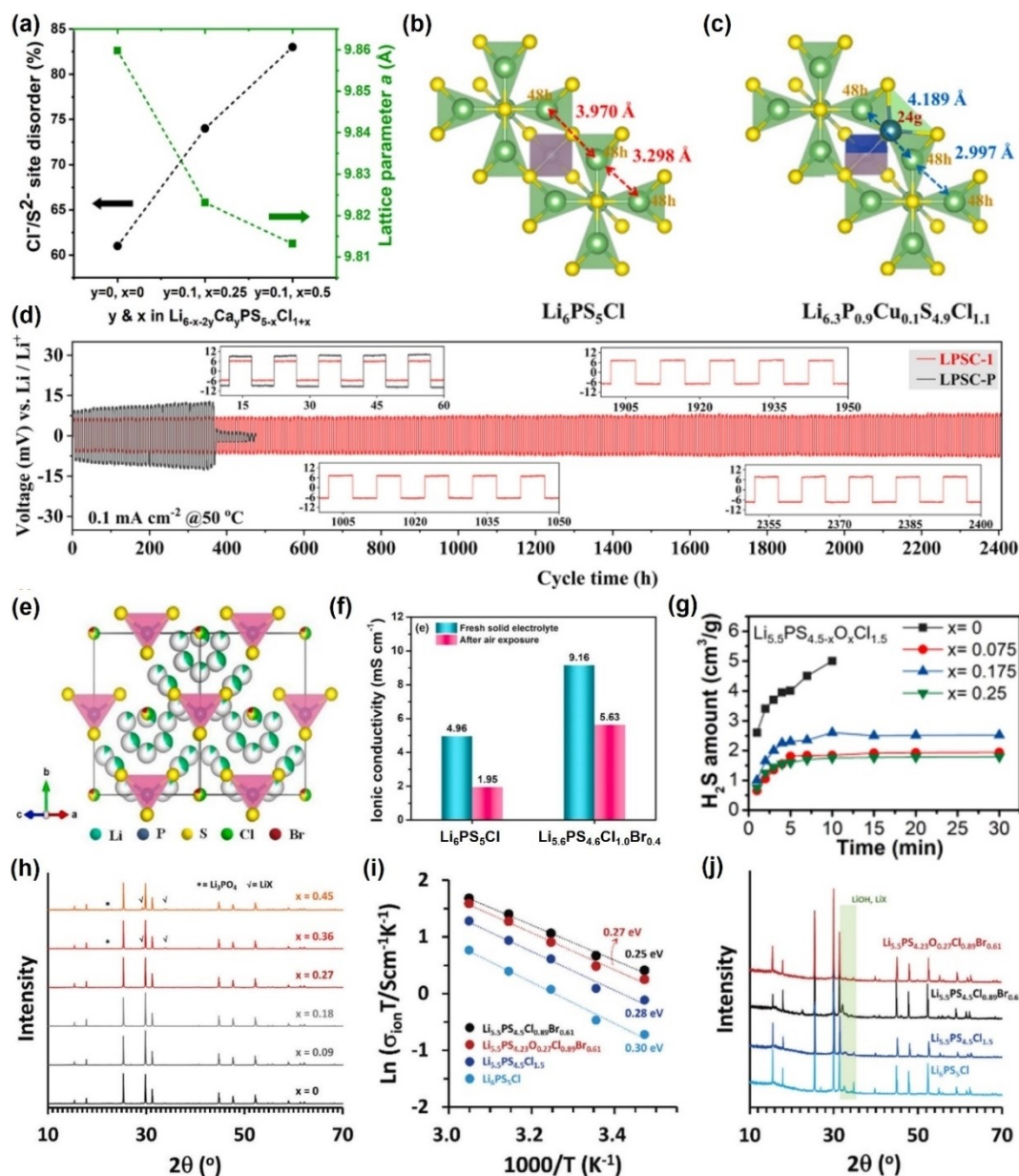
Figure 3. a) Site disorder and lattice parameter vs. x for $Li_{6-x-2y}Ca_yPS_{5-x}Cl_{1+x}$. Reproduced with permission from Ref. [47]. Copyright (2020) American Chemical Society. The Li migration path in b) Li_6PS_5Cl and c) $Li_{6.3}P_{0.9}Cu_{0.1}S_{4.9}Cl_{1.1}$ via DFT calculation. d) Symmetric cell Li|SE|Li configuration for pristine (LPSC–P, black) and 0.1 CuCl doped (LPSC-1, red) at 0.1 mA cm^{-2} current density under 50°C. Reproduced with permission from Ref. [65]. Copyright (2021) Elsevier. e) Crystal structure of optimized $Li_{5.6}PS_{4.6}Cl_{1.0}Br_{0.4}$ solid electrolyte. f) Comparison of ionic conductivity values of Li_6PS_5Cl and $Li_{5.6}PS_{4.6}Cl_{1.0}Br_{0.4}$ solid electrolytes before and after the air stability test. Reproduced with permission from Ref. [45]. Copyright (2022) Elsevier. g) Amount of H_2S gas generated from pelletized $Li_{5.5}PS_{4.5-x}O_xCl_{1.5}$ ($x=0$, 0.075, 0.175, and 0.25) solid electrolytes. The humidity is 20%. Reproduced with permission from Ref. [67]. Copyright (2022) American Chemical Society. h) XRD patterns of $Li_{5.5}PS_{4.5-x}O_xCl_{0.89}Br_{0.61}$ ($x=0$, 0.09, 0.18, 0.27, 0.36, and 0.45). i) Arrhenius plots for various argyrodites including the PSO-obtained $Li_{5.5}PS_{4.5}Cl_{0.89}Br_{0.61}$ and oxygen-tuned $Li_{5.5}PS_{4.23}O_{0.27}Cl_{0.89}Br_{0.61}$. j) Comparison between XRD patterns following exposure to a humid atmosphere (−15°C, 30 min). Reproduced with permission from Ref. [68]. Copyright (2022) John Wiley and Sons.

lithium ions of one Li_6S group to the nearest neighbor Li_6S group in the LPSC-1 crystal increased significantly from 3.970 to 4.189 Å. Additionally, cyclic voltammetry (CV) and Li–Li symmetric cells were used to assess the electrochemical stability and Li metal compatibility, respectively. The CV data demonstrate that in C-LPSC-1|LPSC-1|In configurations, the decomposition peak current associated with the oxidation of sulfur and phosphorus in orthothiophosphat $(P_{1-x}Cu_x)S_4^{(3+4x)-}$ totally vanished and no decomposition current was seen up to up to

8 V vs. Li/Li$^+$. The addition of Cu(I) strengthens the bridging sulfur bonds(-[S]$_n$-) in the sulfide solid electrolyte site for oxidation/reduction and produces a strong covalent link and stiff framework with S^{2-}. The $(P_{1-x}Cu_x)S_4^{(3+4x)-}$ exhibited extremely high stability on the CV curve, with no oxidation or reduction peaks brought on by the decomposition of the compound. Lithium symmetric cells using LPSC-1 as the solid electrolyte show stable Li plating/stripping behavior for more than 2400 hours at 0.1 mA cm^{-2} current density and smooth

Batteries & Supercaps

Review

doi.org/10.1002/batt.202200553

**Chemistry
Europe**

European Chemical
Societies Publishing

cycling performance even at a high current density of 1 mA cm^{-2} for more than 400 hours, indicating superior interfacial stability with respectable dendrite suppress capability (Figure 3d). LPSC-1 has improved Li metal compatibility due to the addition of Cu as a dopant, which stabilizes the SE|Li interface without seriously affecting the (P/Cu)S$_4^{3-}$ structure. More interestingly, the chemical stability and the capability of suppressing H$_2$S generation are also enhanced in CuCl-doped LPSC-1 due to Cu's soft acid properties.

Improved air stability is critical for practical applications of sulfide electrolytes. In addition to soft acid ion doping, the strategies to enhance the air stability of halogen-rich lithium argyrodite electrolytes include halogen mixing and oxygen doping. In order to create a halogen-rich argyrodite framework with the triple advantages of strong phase stability, high Li-conductivity, and low activation energy, Patel et al.[37] examined the mixed-halide argyrodites Li$_{6-x}$PS$_{5-x}$ClBr$_x$ ($0 \leq x \leq 0.8$) in 2021 using a combined experimental and computational method. Faster Li-ion transport occurs in Li$_{6-x}$PS$_{5-x}$ClBr$_x$ due to hyper-coordination and coordination entropy caused by the variety of anion species and Li shortage in halogen-rich Li$_{6-x}$PS$_{5-x}$ClBr$_x$. At 25°C, $x = 0.7$ led to the maximum ionic conductivity of 24 mS cm^{-1}. Subramanian et al. then obtained a mixed argyrodite system (Li$_{6-x}$PS$_{5-x}$ClBr$_x$; $0 \leq x \leq 0.5$) rich in halogens using a high-energy dry ball milling technique and heat treatment. Their electrochemical capabilities and air stability were also revealed (Figure 3e). The optimal room temperature ionic conductivity of 9.16 mS cm^{-1} was observed in Li$_{5.6}$PS$_{4.6}$Cl$_{1.0}$Br$_{0.4}$. According to the results of the H$_2$S gas generation test, mixed halogen-rich argyrodites showed greater air stability than pristine ones. Under the same humidity conditions, the Li$_6$PS$_5$Cl electrolyte produced 0.36 cm^3 g^{-1} H$_2$S gas in just 22 min, while the Li$_{5.6}$PS$_{4.6}$ClBr$_{0.4}$ electrolyte only afforded 0.35 cm^3/g at 55 min. The authors only took in account of non-bonded S^{2-} in argyrodites, which readily interact with moisture to form the H$_2$S gases. This reaction can be regulated by replacing S-site in the Li-argyrodites with extra halogen. The excess halogen in Li$_{5.6}$PS$_{4.6}$ClBr$_{0.4}$ replaced the non-bonded S^{2-} with Cl$^-$/Br$^-$, enabling the improvement of stability with respect to oxygen and moisture. XRD patterns tested before and after air exposure show that halogen-rich lithium argyrodites let oxygen into the crystal structure without the crystal structure degrading. After the air stability test, Li$_{5.6}$PS$_{4.6}$ClBr$_{0.4}$'s ionic conductivity dropped from 9.16 to 5.63 mS/cm and Li$_6$PS$_5$Cl's from 4.96 to 1.95 mS cm^{-1} (Figure 3f). Currently, P$_2$O$_5$ is used to partially replace the raw material P$_2$S$_5$ in the preparation of O-substituted Li$_{5.5}$PS$_{4.5-x}$O$_x$Cl$_{1.5}$ ($x = 0$, 0.075, 0.175, and 0.25) solid electrolytes.[67] The samples' ionic conductivities and air stability were carefully compared. When tested in an ambient environment, Li$_{5.5}$PS$_{4.5-x}$O$_x$Cl$_{1.5}$ ($x = 0$, 0.075, 0.175, and 0.25) electrolytes produce the amount of H$_2$S as shown in Figure 3(g). For LPSC-1.5, the level of H$_2$S increases quickly and surpasses the gas sensor's limit in 10 minutes. Since Li$_{5.5}$PS$_{4.5-x}$O$_x$Cl$_{1.5}$ ($x = 0.075$, 0.175, and 0.25) displays significantly less H$_2$S production than the pure material, O-substituted LPSC-1.5 may have better air/moisture stability. Results for ionic conductivity demonstrate that oxygen doping lowers chlorine-rich LPSC-1.5's ionic

conductivity. Surprisingly, the ionic conductivities of Li$_{5.5}$PS$_{4.425}$O$_{0.075}$Cl$_{1.5}$, Li$_{5.5}$PS$_{4.325}$O$_{0.175}$Cl$_{1.5}$, and Li$_{5.5}$PS$_{4.250}$O$_{0.250}$Cl$_{1.5}$ all remained high at 7.15, 6.33, and 5.95 mS cm^{-1}, respectively. Furthermore, even at a high end-of-charge voltage of 4.5 V (vs. Li/Li$^+$), Li$_{5.5}$PS$_{4.425}$O$_{0.075}$Cl$_{1.5}$ exhibited higher electrochemical stability toward LiNi$_{0.8}$Mn$_{0.1}$Co$_{0.1}$O$_2$ (NCM811) cathode.

Shim et al.[68] developed Li$_{5.5}$PS$_{4.23}$O$_{0.27}$Cl$_{0.89}$Br$_{0.61}$ by combining the benefits of mixed halogen and oxygen doping. The ionic conductivity, moisture stability, and electrochemical stability of this novel composition were all well-balanced. First, both the experimental data and AIMD computations revealed that mixed-halide Li$_{5.5}$PS$_{4.5}$Cl$_{0.89}$Br$_{0.61}$ has a higher ionic conductivity than single-halide LPSC-1.5. Increased lattice softness from the partial replacement of Cl with Br (Li$_{5.5}$PS$_{4.5}$Cl$_{1.5} \rightarrow$ Li$_{5.5}$PS$_{4.5}$Cl$_{0.89}$Br$_{0.61}$) contributes to an increase in ionic conductivity. This is fairly consistent with Patel's research findings.[37] Ionic conductivity for Li$_{5.5}$PS$_{4.5}$Cl$_{0.89}$Br$_{0.61}$ is 7.78 mS cm^{-1} at room temperature. Second, to improve the air stability, oxygen was added to Li$_{5.5}$PS$_{4.5}$Cl$_{0.89}$Br$_{0.61}$ (Li$_{5.5}$PS$_{4.5}$Cl$_{0.89}$Br$_{0.61} \rightarrow$ Li$_{5.5}$PS$_{4.23}$O$_{0.27}$Cl$_{0.89}$Br$_{0.61}$). Due to the deteriorating lattice softness and the production of impurities, the O-doped samples show a modest reduction in ionic conductivity. According to XRD patterns, the high oxygen content causes the impurity phases of Li$_3$PO$_4$ and LiX to form when $x \geq 0.36$ (Figure 3h). Thankfully, Li$_{5.5}$PS$_{4.23}$O$_{0.27}$Cl$_{0.89}$Br$_{0.61}$ has considerably higher moisture stability than the electrolytes without O-doping. Despite the small reduction to 6.70 mS cm^{-1} in ionic conductivity, Li$_{5.5}$PS$_{4.23}$O$_{0.27}$Cl$_{0.89}$Br$_{0.61}$ releases around three times less H$_2$S than Li$_6$PS$_5$Cl during the 90-minute H$_2$S generation experiment (Figure 3i). After the moisture-exposure test, the XRD diffraction peaks of Li$_{5.5}$PS$_{4.23}$O$_{0.27}$Cl$_{0.89}$Br$_{0.61}$ were similar to that of the pristine one, while distinctive new peaks of LiOH and LiX appeared in the XRD patterns of the oxygen-free electrolytes (Figure 3j). The results of ionic conductivity and air stability indicate that the oxygen-doped Li$_{5.5}$PS$_{4.23}$O$_{0.27}$Cl$_{0.89}$Br$_{0.61}$ achieves an appropriate balance between ion conduction and moisture resistance. In addition, the Li||Li symmetric cell and Li||Li-(Ni$_{0.9}$Co$_{0.05}$Mn$_{0.05}$)O$_2$ cell with Li$_{5.5}$PS$_{4.23}$O$_{0.27}$Cl$_{0.89}$Br$_{0.61}$ as solid electrolyte exhibit good electrochemical performances, indicating the superior electrochemical stability of Li$_{5.5}$PS$_{4.23}$O$_{0.27}$Cl$_{0.89}$Br$_{0.61}$.

5. ASSBs with halogen-rich lithium argyrodite electrolytes

Generally, the lithium argyrodite electrolytes exhibit better electrochemical stability than the thermodynamical calculation results due to the passivating effect of the by-products at the electrode/electrolyte interface. As a result, this type of electrolyte can be matched to high voltage cathode and lithium metal anode to construct all-solid-state batteries without any interfacial treatment.[69–75] However, the untreated cathode/electrolyte interface is only stable at low cathode loadings, and the pure lithium metal/electrolyte interface can only tolerate low current densities and short cycle duration.[43,76,77] The interface

impedance increases and contact failure resulting from the accumulated interfacial side reactions or continuous volume changes of the solid particles are still inevitable when the cathode loading is increased or the cycle time is longer. Resulting in severe degradation of the solid-state battery performance. Therefore, improving the interfacial stability between the halogen-rich lithium argyrodite electrolyte and the electrodes (cathode and anode) remains important for developing high-performance all-solid-state batteries. In this section, the performances of halogen-rich lithium argyrodite-based all-solid-state batteries without any interface treatment are presented. The strategies for improving the electrode/electrolyte solid-solid interface stability are introduced. In addition, the fabrication processes of ASSBs with halogen-rich lithium argyrodite electrolytes have been sorted out.

5.1. Cathode/SE interface & improvement

Recently, we constructed SSBs employing LPSC-1.5 electrolyte, pristine $LiNi_{0.6}Co_{0.2}Mn_{0.2}O_2$ (NCM622) cathode, and Li–In anode to evaluate the electrochemical stability between LPSC-1.5 solid electrolyte and pristine oxide cathode. At 5 C, the assembled SSB had a capacity of 102.8 mAh g^{-1}, and after 4500 cycles at room temperature, it still had 99.4% of its original capacity. Surprisingly, the battery managed to stably cycle 10000 times at 10 C with a remarkable capacity retention of 82.4% (Figure 4a).[43] The battery's resistance increased slightly by 50 Ω after 10,000 cycles at 10 C, according to the EIS measurements, demonstrating rapid lithium-ion migration dynamics at the

LPSC-1.5/NCM622 interface. The interface's low activation energy was also demonstrated in our earlier efforts. Additionally, because of the LPSC-1.5 electrolyte's high conductivity, the aforementioned ASSB can function reliably at −20 °C. The findings demonstrate chlorine-rich lithium argyrodite's enormous potential for creating high-performance SSBs devoid of any electrolyte/cathode interface pretreatment. However, the modifications for the electrolyte/electrode interface are still necessary to meet the needs of practical applications, such as higher cathode loading, larger C-rate, and longer cycling duration.

Cathode coating is an efficient strategy to stabilize the oxide cathode/sulfide electrolyte interface. For this view, we explored the influence of the $LiNbO_3$ (LNO) layer on the electrochemical performances of the SSBs with $LiNi_{0.7}Co_{0.1}Mn_{0.2}O_2$ (NCM712) and choline-rich LPSC-1.5 as cathode and solid electrolyte, respectively.[78] The SSBs using $LiNbO_3$-coated NCM712 (LNO@NCM712) exhibited comparable electrochemical performance at a low rate (0.1 C) compared to that with pristine NCM712 electrode. However, at high rates and high temperatures, the coating's impact on battery performance is evident. LNO@NCM712 displays significantly improved discharge capacity and significantly less polarization at higher charge/discharge rates. While the ASSBs employing the original NCM712 have significantly lower first discharge capacities and capacity retentions under the same cycling settings, the ones with LNO@NCM712 do give high initial capacities at 5 C under RT and 60 °C with exceptional capacity retentions of 87.5% and 88% after 600 and 300 cycles (Figure 4b). In the pristine NCM712 composite cathode, consid-
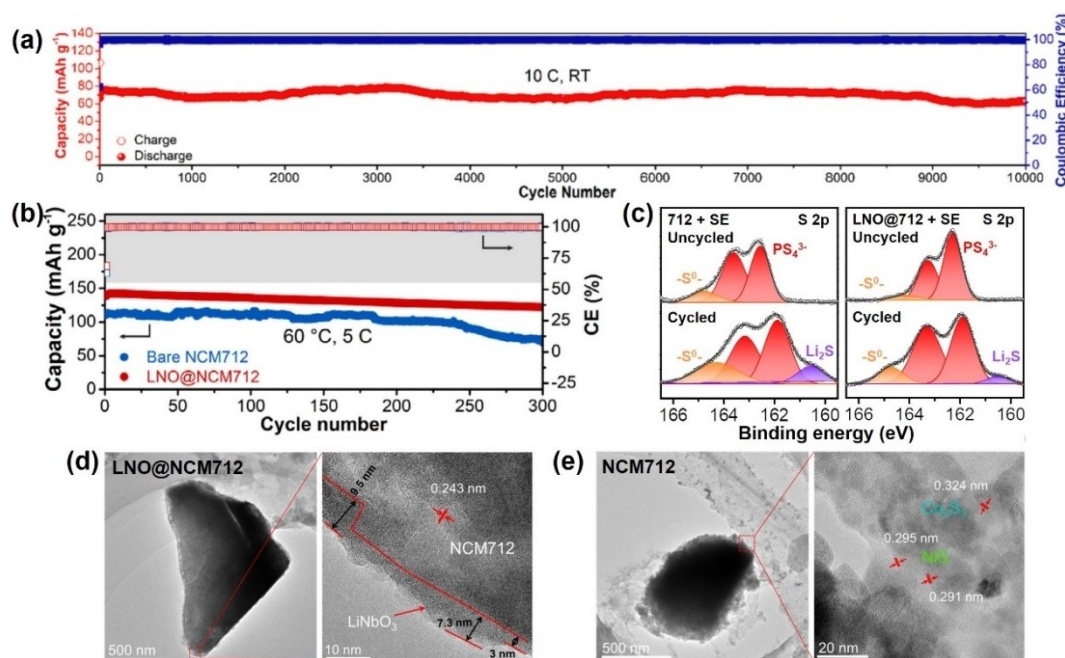

Figure 4. a) Capacity of Li∣∣LNO@NCM622 cell for the first 30 cycles run at 0.1 mA cm^{-2} at 24±4 °C using LPSC-1.3 SE. Reproduced with permission from Ref. [43]. Copyright (2022) Elsevier. b) Cycle performance and CE changes of the $LiNi_{0.7}Mn_{0.2}Co_{0.1}O_2$(NCM712)/LPSC-1.5/In–Li SSBs using the pristine and coated NCM712 electrodes cycled at 5 C at 60 °C. c) The corresponding XPS of the NCM712 and LNO@NCM712 electrodes before and after cycles. TEM of the d) NCM712 and e) LNO@NCM712 electrodes after 300 cycles at 5 C under 60 °C. Reproduced with permission from Ref. [78]. Copyright (2022) Elsevier.

Batteries & Supercaps

Review
doi.org/10.1002/batt.202200553

Chemistry Europe
European Chemical
Societies Publishing

erably higher Li_2S and polysulfide P_2S_x as decomposition species are found by XPS after 300 cycles at 5 C below 60 °C (Figure 4c). On the other hand, fewer by-products are found in the LNO@NCM712 composite electrode, showing that the LNO coating layer effectively prevents the decomposition of LPSC-1.5. TEM results show that the cycled LNO@NCM712 materials maintain a similar particle size to the fresh one, despite the LNO layer turning uneven in thickness due to the tiny side reactions (Figure 4d). However, for the pristine NCM712 electrode without the protection of the LNO coating layer, much smaller particle sizes and obvious transition metal sulfides (NiS (100) and MnS (111)) are observed after cycling (Figure 4e). The cracked particles formed are due to the volume changes during cycling, while the transition metal sulfides are derived from the side reaction between the NCM712 cathode and LPSC-1.5 electrolyte. The LNO coating layer plays a key role in relieving interfacial side reactions and cathode volume changes contribute to the excellent electrochemical performance of the ASSBs. Moreover, the coated NCM712 electrode exhibits much better low-temperature performance, attributed to the fast ion transport kinetics in interface and bulk provided by the coating layer and the chlorine-rich argyrodite electrolyte with high ionic conductivity.

In addition, halide electrolytes with high oxide cathode stability have received a lot of attention in recent years.[30,31,35,79,80] It is a promising strategy to employ the halides as an electrolyte additive in the composite cathode or as a buffer layer to separate the oxide cathode and sulfide electrolyte.[81] Our group has introduced halide SE into a halogen-rich argyrodite electrolyte-based system for constructing high-performance ASSBs. The results will be discussed in a later section.

5.2. Li-metal/SE interface & improvement

The interfacial interactions between Li-metal and argyrodite electrolytes with varying chlorine contents ($Li_{7-x}PS_{6-x}Cl_x$, $x = 0.6$, 1.0, 1.3, 1.45, and 1.6) were thoroughly studied by Zeng et al.[76] In terms of microstructure, interphase composition, and morphology, they suggested that the Cl distribution and chilling procedure used during the SE synthesis have a significant impact on how the interface evolves. The patterns of impedance change over time for $Li|Li_{7-x}PS_{6-x}Cl_x|Li$ symmetric cells were carried out to evaluate the impact of chlorine content on the chemical stability between the electrolyte and lithium metal. The results show a negative correlation between the increase in interfacial impedance and the chlorinity, $Li|Cl$-16$|Li$ symmetric cell with the smallest increase in impedance after 600 h. This suggests that increasing the chlorine content can mitigate interfacial reactions between argyrodite electrolytes and lithium metal. However, the Li plating/stripping behavior of $Li|Li_{7-x}PS_{6-x}Cl_x|Li$ symmetric cells indicates that Cl-13 with a maximum critical current density (CCD) over 1 mA cm^{-2}. While Cl-16 exhibits the lowest CCD (0.56 mA cm^{-2}), even lower than that of Cl-06. The electrochemical performances of $Li|SE|LNO@NCM622$ employing Cl-13 and Cl-06 were

also investigated. The former displays higher initial Coulombic efficiency, better cycling stability, and lower polarization voltages, suggesting superior interfacial compatibility between the Cl-13 and Li anode (Figure 5a). XPS, SEM, and Cryo-STEM were conducted for analyzing the differences in the interface regions of the $Li|Li_{7-x}PS_{6-x}Cl_x|Li$ ($x = 0.6$, 1.3) symmetric cells after Li plating/stripping for 200 cycles and deciphering the behind mechanism. The XPS results show that Cl-06 is decomposed to Li_2S, P-based phases, Li_3P, and the rarely observed Li_2S_n. For Cl-13, Li_2S_n is absent, and the amounts of all decomposition products are much lower than those of Cl-06 (Figure 5b). Li_2S_n is induced by a low chlorinity with a higher electronic conductivity but lower ionic conductivity than Li_2S. Furthermore, a compact and even LiCl-dominated layer forms at Li/Cl-13 surface after cycling, while the layer is irregular and uneven in Cl-06. This phenomenon stems from different distributions of chlorine atoms in the electrolytes. On the S sites for Cl-06, all Cl atoms are successfully replaced. Even so, the Cl atoms in Cl-13 and Cl-16 largely exist on the surface of each grain by producing a shell layer of nanoscale. These shell layers connect to one another and build a framework. To achieve successful doping, only a portion of Cl atoms must reside inside the argyrodite lattice. Notably, Cl-13's nanoshell (20 nm) is narrower than Cl-16's (50 nm, Figure 5c). Cl ions in the nanoshells go to the Li electrode surface under the electric field during the electrochemical cycling and rebind with Li ions to generate a LiCl-dominant interphase layer. The transit of the Cl ions is impeded by the thick LiCl nanoshell in Cl-16. As a result, argyrodite electrolytes have the best electrochemical stability with mild chlorinity.

The LiCl nanoshell in Cl-rich argyrodite electrolytes may be an effective factor to stabilize the argyrodite electrolytes/ lithium metal interface. However, the uniformity of distribution and thickness of the LiCl nanoshell is difficult to ensure, making it challenging to achieve the long-cycle stability of SSBs. To achieve long-term stable operation of SSBs using a lithium metal anode, Ye et al.[77] designed a LPSC-1.5-LGPS-LPSC-1.5 "sandwich" multilayer electrolyte. The authors have experimentally demonstrated that the sulfide solid electrolytes, which have fewer side reactions with lithium metal, are instead more susceptible to penetration by lithium dendrites. The reason is that during the charging and discharging of the battery, the lithium dendrites easily penetrate through the micro-cracks in the electrolyte layer, causing a short circuit. In contrast, the electrolytes that are more prone to react with lithium metal (e.g., LGPS) will partially decompose during cycling. However, local pressure or sub-stable interfaces would prevent this decomposition process from further occurring. The whole process is similar to the "expansion screw effect", which effectively inhibits the penetration of lithium dendrites and ensures the long-cycle stability of solid-state lithium metal batteries. Because of this mechanism, the assembled Li–Li symmetric cell with LPSC-1.5-LGPS-LPSC-1.5 "sandwich" multilayer electrolyte showed smooth Li plating/stripping behavior and high CCD of 20 mA cm^{-2}. After a long period of cycling, the LPSC-1.5 layer formed a large number of obvious cracks, while the LGPS layer was denser (Figure 5d). Moreover, a clear
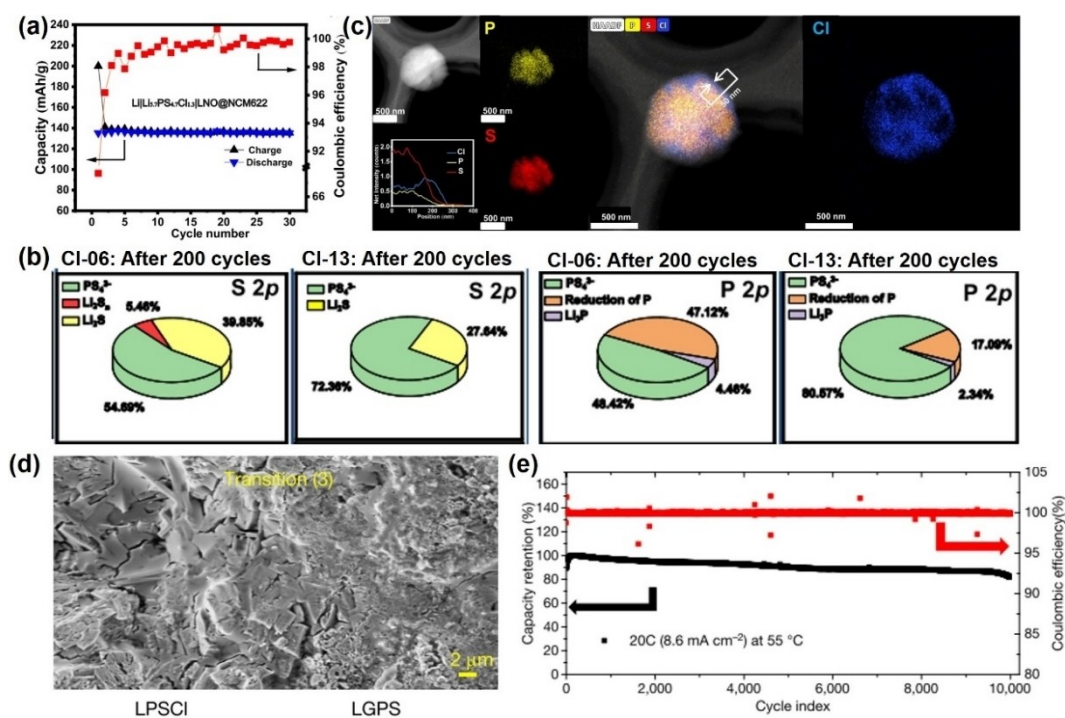
Batteries & Supercaps

Review
doi.org/10.1002/batt.202200553

Chemistry
Europe
European Chemical
Societies Publishing

Figure 5. a) Capacity of Li‖LNO@NCM622 cell for the first 30 cycles run at 0.1 mA cm^{-2} at 24±4 °C using Cl-13 SE. b) XPS semi-quantitative analyses on Li|SE interface for Li‖Li symmetric cells using Cl-06 and Cl-13 SEs after Li plating/stripping for 200 cycles. c) Cryogenic STEM-HAADF and EDS images of as-prepared Cl-16 powder. Reproduced with permission from Ref. [76]. Copyright (2022) Springer Nature. d) SEM images of different cross-section regions of the multilayer on LPSCl-LGPS transition areas. e) Capacity retention of the battery cycled over 10000 cycles at a rate of 20 C with the voltage range 2.0–4.35 V at 55 °C. Reproduced with permission from Ref. [77]. Copyright (2021) Springer Nature.

transition region had been observed at the interface between the two electrolyte layers, which can be explained by the "expansion screw effect" mentioned above. A similar phenomenon was also found by McDowell et al. in the Li_6PS_5Cl-$Li_{10}SnP_2S_{12}$-Li_6PS_5Cl system. Subsequently, the NCM811/LPSC-1.5-LGPS-LPSC-1.5/G—Li ASSB constructed with this multilayer electrolyte was stable for 10000 cycles at a high C-rate of 20.0 C with a capacity retention rate of 82.0% (Figure 5e). The novel design strategy demonstrates the great potential of chlorine-rich lithium argyrodite electrolytes in the construction of long-cycle lithium metal SSBs.

Forming stable SEI by elemental doping is efficient for stabilizing the sulfide electrolyte/lithium metal interface but will reduce the ionic conductivity of SE. The halogen-rich argyrodite electrolytes with high ionic conductivity have the potential to achieve a balance between ionic conductivity and lithium metal compatibility by doping. It is an approach worth exploring to enhance the electrochemical stability between halogen-rich argyrodite electrolytes and lithium metal.

5.3. Fabrication process of ASSBs

ASSBs employing thin solid electrolyte layers facilitate higher energy densities, which is a necessary part of driving the practical applications of ASSBs. The following paper focuses on the halogen-rich argyrodite electrolyte films prepared by liquid-

phase and dry-mixing processes and their applications in ASSBs.

Xia et al.[82] designed a novel integrated electrode structure by coating the LPSC-1.5-xNBR electrolyte slurry onto the surface of the obtained dried NCM811 cathode (Figure 6a). Toluene and butyl butyrate were chosen as solvents because of their compatibility with argyrodite electrolytes. The conformal in-situ integration of sulfide solid electrolyte with oxide cathode is favorable to their intimate contact, resulting in a robust solid-solid interface and decreased interfacial resistances. As a result, the assembling ASSBs exhibited superior cycle and rate performances than that with segregated structures (Figure 6b and c). The EIS results of the two types of ASSBs showed that the LPSC-1.5-3NBR-integrated NCM811 cathode‖Li cell demonstrates a smaller charge-transfer resistance of the cathode/solid electrolyte interface. The smaller charge-transfer resistance contributes to higher electronic conductivity and faster ionic migration on the interface between the solid electrolyte and the cathode. In addition, the thickness of the LPSC-1.5-3NBR electrolyte layer can be controlled at about 50 μm, which is thinner than other electrolyte films fabricated by the tape casting method. Fortunately, it maintained a high ionic conductivity of over 10^{-3} S cm^{-1}. The thin electrolyte layers are beneficial for the construction of high-energy-density ASSBs.

The organic solvents introduced in the liquid phase method are difficult to remove completely and inevitably lead to inferior ionic conductivity of the solid electrolyte. Given this, researchers have attempted to prepare electrolyte membranes
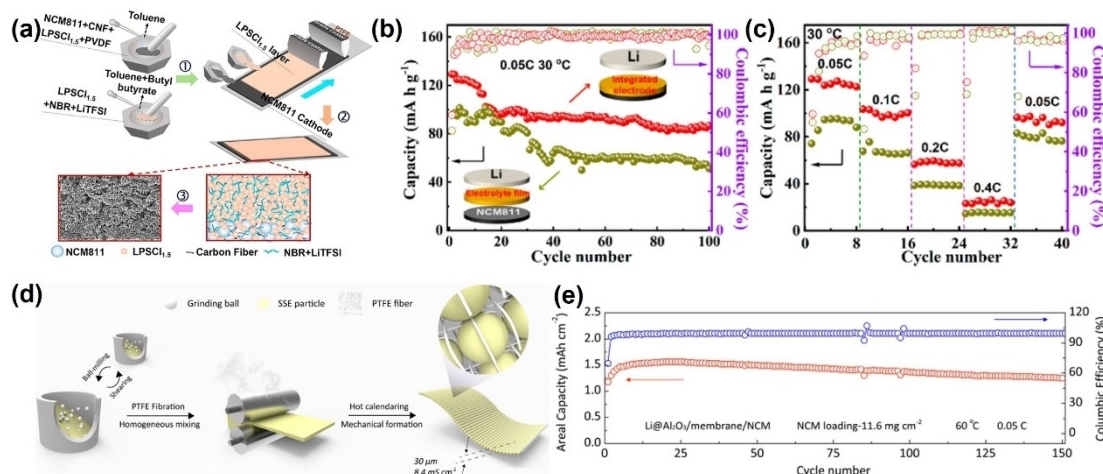
Batteries & Supercaps

Review
doi.org/10.1002/batt.202200553

Chemistry Europe
European Chemical
Societies Publishing

Figure 6. a) Schematic illustration of the sulfide solid electrolyte integrated Ni-rich oxide cathode. Electrochemical performance of the LPSC-1.5-3NBR electrolyte-integrated NCM811 cathode||Li cell and NCM811||LPSC-1.5-3NBR||Li cell: b) cycling performance and c) C-rate performance. Reproduced with permission from Ref. [82]. Copyright (2022) American Chemical Society. d) Schematic illustration of the ultrathin SE membrane fabrication. e) Cyclic performance of the NCM/Li ASSLB with a high NCM mass loading of 11.6 mg cm^{-2} at 0.05 C (0.085 mA cm^{-2}). Reproduced with permission from Ref. [83]. Copyright (2021) American Chemical Society.

using a dry-mix process. During the preparation of sulfide electrolyte films by dry blending, a small amount of polymer is usually added as a binder, and PTFE is one of the common binders. Recently, Zhang et al.[83] mixed LPSC-1.6 (99.8 wt.%) and PTFE (0.2 wt.%) powder followed by pressing the mixture together to get a freestanding and continuous solid electrolyte film (Figure 6d). The electrolyte film displayed good mechanical properties even with a thickness of 30 μm, due to the PTFE fibers forming a matrix supporting the LPSC-1.6 particles. Furthermore, the electrolyte film exhibited high room temperature ionic conductivity of up to 8.4 mS cm^{-1} resulting from the ultrahigh conductivity of LPSC-1.6 powder (10.8 mS cm^{-1}). This value represents the highest level of ionic conductivity of reported electrolyte membranes to date. Subsequently, the LPSC-1.6 film was assembled into an ASSB with NCM523 and Al$_2$O$_3$-coated Li-metal as cathode and anode respectively. The ASSB exhibited excellent cycling stability of capacity retention of 80.2% for 150 cycles under 60°C due to the good mechanical stability and outstanding electrochemical properties of the electrolyte film (Figure 6e). Table 3 summarizes the parameters of different argyrodite electrolyte films.

6. Conclusion and Perspectives

This review systematically introduces the development process of halogen-rich lithium argyrodite electrolytes in recent years in terms of crystal structure, ion conduction mechanism, synthesis routes, modification strategy, electrode/electrolyte interface improvement, and construction of ASSB. This type of solid electrolyte can reach a high ionic conductivity of 10^{-2} S cm^{-1} by tuning the halide content. In addition, the electrolyte has relatively good electrochemical stability and a relatively low cost compared to other sulfide electrolytes. All these properties make it one of the most promising sulfide electrolytes. However, there are still many challenges that need to be addressed to advance its practical application.

1) The influence mechanisms of different halogen contents. Tuning halogen content in argyrodite structure not only affects the ionic conductivity of the electrolyte but also its air and electrochemical stabilities. The mechanism of improving the air stability and electrochemical stability of argyrodite electrolytes by different halogen contents or mixed halogens needs to be further investigated. The study of the effect of halogen content on argyrodite crystal structure is important.

2) Modification of doping. The halogen-rich lithium argyrodite electrolytes have a sufficiently high ionic conductivity that there is no concern about reduced ionic conductivity caused by elemental doping. More elemental doping strategies can be tried to enhance their air stability, and compatibilities with oxide cathode and Li-metal anode, and to develop a SE with generally superior performance. In addition, blending functional additives with electrolytes is also a means of improving their comprehensive performance.

3) Preparation on a large scale. At present, the synthesis methods of halogen-rich lithium argyrodite electrolytes are

Table 3. The parameters of different argyrodite electrolyte films.

SE film	σ_{rt} [mS/cm]	Thickness [μm]	Synthesis route	Ref.
LPSC-1.5	1.4	50	liquid-phase	[82]
LPSC-1.6	8.4	30	dry-mix	[83]
LPSC-1.0	6.3	60	liquid-phase	[84]

The results prove halogen-rich argyrodite electrolytes are a promising candidate for preparing sulfide electrolyte membranes with high ionic conductivity and excellent electrochemical performances.

Batteries & Supercaps

Review
doi.org/10.1002/batt.202200553

Chemistry Europe
European Chemical
Societies Publishing

still relatively complicated and demanding. It is necessary to design a facile and efficient synthesis route that is highly reproducible and suitable for large-scale preparation, to guarantee its large-scale application in ASSBs. The solid-phase synthesis method can be considered to avoid the high-speed ball milling process, while the liquid-phase method requires searching for a suitable solvent.

4) Electrolyte film. The thinner the electrolyte layer, the higher the energy density. Electrolyte film is key to constructing high-energy-density ASSB. The ultra-high ionic conductivity of halogen-rich lithium argyrodite electrolytes gives them great potential to prepare high-performance electrolyte films. Therefore, a suitable solvent or binder for halogen-rich lithium argyrodite electrolytes should be explored to fabricate high-performance electrolyte films. Additionally, compounding halogen-rich lithium argyrodite electrolytes with polymers is a promising strategy.

5) Introducing a double-layer electrolyte inside the solid-state battery. In the construction of an all-solid-state battery, the introduction of a more stable electrolyte in the cathode mix instead of the sulfide electrolyte can play the role of a "lithium-ion additive" and also isolate the electrolyte from direct contact with the high-voltage active material to avoid side reactions. The introduction of another electrolyte buffer layer between the cathode layer and the argyrodite electrolyte layer also prevents side reactions from occurring. The graded use of electrolytes within the solid-state battery can effectively suppress side reactions and enhance the lithium ion transfer rate and efficiency, thus realizing the construction of a high-performance all-solid-state battery.

6) Optimization of the solid-state battery assembly process. Combining the assembly process of solid-state batteries with the current liquid battery preparation process, and designing a suitable preparation process and route for all-solid-state batteries based on current battery assembly equipment is of great significance to reduce the cost of solid-state batteries and promote their practical progress. The high ionic conductivity and relatively low cost of halogen-rich lithium argyrodite electrolytes offer opportunities for their large-scale application, but the challenges posed by their sulfide properties remain, and the joint efforts of academia and industry are still needed to promote their application in solid-state batteries.

Acknowledgements

Conflict of Interest

The authors declare that they have no known competing financial interests or personal relationships that could have appeared to influence the work reported in this paper.

[1] Z. Gao, H. Sun, L. Fu, F. Ye, Y. Zhang, W. Luo, Y. Huang, *Adv. Mater.* **2018**, *30*, e1705702.
[2] H. Lee, P. Oh, J. Kim, H. Cha, S. Chae, S. Lee, J. Cho, *Adv. Mater.* **2019**, *31*, e1900376.
[3] P. Oh, H. Lee, S. Park, H. Cha, J. Kim, J. Cho, *Adv. Energy Mater.* **2020**, *10*, e2000904.
[4] Q. Zhang, D. X. Cao, Y. Ma, A. Natan, P. Aurora, H. L. Zhu, *Adv. Mater.* **2019**, *31*, e1901131.
[5] J. C. Bachman, S. Muy, A. Grimaud, H. H. Chang, N. Pour, S. F. Lux, O. Paschos, F. Maglia, S. Lupart, P. Lamp, L. Giordano, Y. Shao-Horn, *Chem. Rev.* **2016**, *116*, 140–162.
[6] H. Yuan, J. Liu, Y. Lu, C. Z. Zhao, X. B. Cheng, H. X. Nan, Q. B. Liu, J. Q. Huang, Q. Zhang, *Chem. Res. Chin. Univ.* **2020**, *36*, 377–385.
[7] J. H. Wu, L. Shen, Z. H. Zhang, G. Z. Liu, Z. Y. Wang, D. Zhou, H. L. Wan, X. X. Xu, X. Y. Yao, *Electrochem. Energy Rev.* **2020**, *4*, 101–135.
[8] S. J. Chen, D. J. Xie, G. Z. Liu, J. P. Mwizerwa, Q. Zhang, Y. R. Zhao, X. X. Xu, X. Y. Yao, *Energy Storage Mater.* **2018**, *14*, 58–74.
[9] J. Schnell, H. Knorzer, A. J. Imbsweiler, G. Reinhart, *Energy Technol-Ger.* **2020**, *8*, 1901237.
[10] C. Singer, J. Schnell, G. Reinhart, *Energy Technol-Ger.* **2020**, *9*, 2000665.
[11] P. J. Lian, B. S. Zhao, L. Q. Zhang, N. Xu, M. T. Wu, X. P. Gao, *J. Mater. Chem. A* **2019**, *7*, 20540–20557.
[12] C. Zheng, L. Li, K. Wang, C. Wang, J. Zhang, Y. Xia, H. Huang, C. Liang, Y. Gan, X. He, X. Tao, W. Zhang, *Batteries & Supercaps* **2020**, *4*, 8–38.
[13] H. Jia, X. Liang, T. An, L. Peng, J. Feng, J. Xie, *Chem. Mater.* **2020**, *32*, 4065–4071.
[14] Q. Zhao, S. Stalin, C.-Z. Zhao, L. A. Archer, *Nat. Rev. Mater.* **2020**, *5*, 229–252.
[15] M. Cronau, M. Duchardt, M. Szabo, B. Roling, *Batteries & Supercaps* **2022**, *5*, e202200041.
[16] A. Manthiram, X. Yu, S. Wang, *Nat. Rev. Mater.* **2017**, *2*, 16103.
[17] Z. Zhang, Y. Shao, B. Lotsch, Y.-S. Hu, H. Li, J. Janek, L. F. Nazar, C.-W. Nan, J. Maier, M. Armand, L. Chen, *Energy Environ. Sci.* **2018**, *11*, 1945–1976.
[18] V. Thangadurai, S. Narayanan, D. Pinzaru, *Chem. Soc. Rev.* **2014**, *43*, 4714.
[19] K. K. Fu, Y. H. Gong, B. Y. Liu, Y. Z. Zhu, S. M. Xu, Y. G. Yao, W. Luo, C. W. Wang, S. D. Lacey, J. Q. Dai, Y. N. Chen, Y. F. Mo, E. Wachsman, L. B. Hu, *Sci. Adv.* **2017**, *3*, e1601659.
[20] X. Bai, Y. Duan, W. Zhuang, R. Yang, J. Wang, *J. Mater. Chem. A* **2020**, *8*, 25663.
[21] C. Yu, F. Zhao, J. Luo, L. Zhang, X. Sun, *Nano Energy* **2021**, *83*, 105858.
[22] N. Kamaya, K. Homma, Y. Yamakawa, M. Hirayama, R. Kanno, M. Yonemura, T. Kamiyama, Y. Kato, S. Hama, K. Kawamoto, A. Mitsui, *Nat. Mater.* **2011**, *10*, 682–686.
[23] Y. Kato, S. Hori, T. Saito, K. Suzuki, M. Hirayama, A. Mitsui, M. Yonemura, H. Iba, R. Kanno, *Nat. Energy* **2016**, *1*, 16030.
[24] C. Li, S. Zhang, X. Miao, C. Wang, C. Wang, Z. Zhang, R. Wang, L. Yin, *Batteries & Supercaps* **2021**, *5*, 14–39.
[25] X. Yang, X. Gao, M. Jiang, J. Luo, J. Yan, J. Fu, H. Duan, S. Zhao, Y. Tang, R. Yang, R. Li, J. Wang, H. Huang, C. Veer Singh, X. Sun, *Angew. Chem. Int. Ed.* **2023**, *62*, e202215680.
[26] C. Li, R. Liu, S. Zhang, Q. Li, C. Wang, Z. Zhang, C. Wang, L. Yin, R. Wang, *Chin. Chem. Lett.* **2022**, doi.org/10.1016/j.cclet.2022.108083.
[27] J. Wu, S. Liu, F. Han, X. Yao, C. Wang, *Adv. Mater.* **2020**, e2000751.
[28] Y. Z. Zhu, Y. F. Mo, *Angew. Chem. Int. Ed.* **2020**, *59*, 17472–17476; *Angew. Chem.* **2020**, *132*, 17625–17629.
[29] E. Umeshbabu, B. Zheng, Y. Yang, *Electrochem. Energy Res.* **2019**, *2*, 199–230.

[30] X. Li, J. Liang, X. Yang, K. R. Adair, C. Wang, F. Zhao, X. Sun, *Energy Environ. Sci.* **2020**, *13*, 1429–1461.

[31] J. Liang, X. Li, K. R. Adair, X. Sun, *Acc. Chem. Res.* **2021**, *54*, 1023–1033.

[32] Q. Zhang, K. Liu, F. Ding, X. Liu, *Nano Res.* **2017**, *10*, 4139–4174.

[33] Q. Zhou, J. Ma, S. Dong, X. Li, G. Cui, *Adv. Mater.* **2019**, *31*, e1902029.

[34] Y. Lee, J. Jeong, H. J. Lee, M. Kim, D. Han, H. Kim, J. M. Yuk, K.-W. Nam, K. Y. Chung, H.-G. Jung, S. Yu, *ACS Energy Lett.* **2021**, *7*, 171–179.

[35] A. Gautam, M. Ghidiu, E. Suard, M. A. Kraft, W. G. Zeier, *ACS Appl. Energ. Mater.* **2021**, *4*, 7309–7315.

[36] Y. Liu, H. Peng, H. Su, Y. Zhong, X. Wang, X. Xia, C. Gu, J. Tu, *Adv. Mater.* **2022**, *34*, e2107346.

[37] S. V. Patel, S. Banerjee, H. Liu, P. Wang, P.-H. Chien, X. Feng, J. Liu, S. P. Ong, Y.-Y. Hu, *Chem. Mater.* **2021**, *33*, 1435–1443.

[38] P. Wang, H. Liu, S. Patel, X. Feng, P.-H. Chien, Y. Wang, Y.-Y. Hu, *Chem. Mater.* **2020**, *32*, 3833–3840.

[39] P. Adeli, J. D. Bazak, K. H. Park, I. Kochetkov, A. Huq, G. R. Goward, L. F. Nazar, *Angew. Chem. Int. Ed.* **2019**, *58*, 8681–8686; *Angew. Chem.* **2019**, *131*, 8773–8778.

[40] T. T. Zuo, F. Walther, J. H. Teo, R. Ruess, Y. Wang, M. Rohnke, D. Schroder, L. F. Nazar, J. Janek, *Angew. Chem. Int. Ed.* **2022**, *3*, e202213228.

[41] K. J. Kim, M. Balaish, M. Wadaguchi, L. Kong, J. L. M. Rupp, *Adv. Energy Mater.* **2020**, *11*, 2002689.

[42] Y. Liu, H. Su, Y. Zhong, X. Wang, X. Xia, C. Gu, J. Tu, *Adv. Funct. Mater.* **2022**, *32*, 2207978.

[43] L. Peng, C. Yu, Z. Zhang, H. Ren, J. Zhang, Z. He, M. Yu, L. Zhang, S. Cheng, J. Xie, *Chem. Eng. J.* **2022**, *430*, 132896.

[44] X. Feng, P.-H. Chien, Y. Wang, S. Patel, P. Wang, H. Liu, M. Immediato-Scuotto, Y.-Y. Hu, *Energy Storage Mater.* **2020**, *30*, 67–73.

[45] Y. Subramanian, R. Rajagopal, K.-S. Ryu, *J. Power Sources* **2022**, *520*, 230849.

[46] H.-J. Deiseroth, S.-T. Kong, H. Eckert, J. Vannahme, C. Reiner, T. Zaiß, M. Schlosser, *Angew. Chem. Int. Ed.* **2008**, *120*, 767–770.

[47] P. Adeli, J. D. Bazak, A. Huq, G. R. Goward, L. F. Nazar, *Chem. Mater.* **2020**, *33*, 146–157.

[48] N. J. J. de Klerk, I. Rosłoń, M. Wagemaker, *Chem. Mater.* **2016**, *28*, 7955–7963.

[49] R. Schlenker, A.-L. Hansen, A. Senyshyn, T. Zinkevich, M. Knapp, T. Hupfer, H. Ehrenberg, S. Indris, *Chem. Mater.* **2020**, *32*, 8420–8430.

[50] A. R. Stamminger, B. Ziebarth, M. Mrovec, T. Hammerschmidt, R. Drautz, *Chem. Mater.* **2019**, *31*, 8673–8678.

[51] C. Yu, Y. Li, M. Willans, Y. Zhao, K. R. Adair, F. Zhao, W. Li, S. Deng, J. Liang, M. N. Banis, R. Li, H. Huang, L. Zhang, R. Yang, S. Lu, Y. Huang, X. Sun, *Nano Energy* **2020**, *69*, 104396.

[52] C. Yu, Y. Li, W. Li, K. R. Adair, F. Zhao, M. Willans, J. Liang, Y. Zhao, C. Wang, S. Deng, R. Li, H. Huang, S. Lu, T.-K. Sham, Y. Huang, X. Sun, *Energy Storage Mater.* **2020**, *30*, 238–249.

[53] C. Liao, C. Yu, X. Miao, S. Chen, L. Peng, C. Wei, Z. Wu, S. Cheng, J. Xie, *Materialia* **2022**, *26*, 101603.

[54] L. Zhou, K.-H. Park, X. Sun, F. Lalère, T. Adermann, P. Hartmann, L. F. Nazar, *ACS Energy Lett.* **2019**, *4*, 265–270.

[55] L. Wu, Z. Zhang, G. Liu, W. Weng, Z. Zhang, X. Yao, *ACS Appl. Mater. Interfaces* **2021**, *13*, 46644–46649.

[56] D. H. Kim, Y. H. Lee, Y. B. Song, H. Kwak, S. Y. Lee, Y. S. Jung, *ACS Energy Lett.* **2020**, *5*, 718–727.

[57] J. E. Lee, K. H. Park, J. C. Kim, T. U. Wi, A. R. Ha, Y. B. Song, D. Y. Oh, J. Woo, S. H. Kweon, S. J. Yeom, W. Cho, K. Kim, H. W. Lee, S. K. Kwak, Y. S. Jung, *Adv. Mater.* **2022**, *34*, e2200083.

[58] D. H. Kim, H. A. Lee, Y. B. Song, J. W. Park, S. M. Lee, Y. S. Jung, *J. Power Sources* **2019**, *426*, 143–150.

[59] N. C. Rosero-Navarro, A. Miura, K. Tadanaga, *J. Power Sources* **2018**, *396*, 33–40.

[60] S. Yubuchi, S. Teragawa, K. Aso, K. Tadanaga, A. Hayashi, M. Tatsumisago, *J. Power Sources* **2015**, *293*, 941–945.

[61] J. Zhang, H. Zhong, C. Zheng, Y. Xia, C. Liang, H. Huang, Y. Gan, X. Tao, W. Zhang, *J. Power Sources* **2018**, *391*, 73–79.

[62] W. Arnold, V. Shreyas, Y. Li, M. K. Koralalage, J. B. Jasinski, A. Thapa, G. Sumanasekera, A. T. Ngo, B. Narayanan, H. Wang, *ACS Appl. Mater. Interfaces* **2022**, *14*, 11483–11492.

[63] Z. Jiang, H. Peng, Y. Liu, Z. Li, Y. Zhong, X. Wang, X. Xia, C. Gu, J. Tu, *Adv. Energy Mater.* **2021**, *11*, 2101521.

[64] T. Chen, D. Zeng, L. Zhang, M. Yang, D. Song, X. Yan, C. Yu, *J. Energy Chem.* **2021**, *59*, 530–537.

[65] B. W. Taklu, W.-N. Su, Y. Nikodimos, K. Lakshmanan, N. T. Temesgen, P.-X. Lin, S.-K. Jiang, C.-J. Huang, D.-Y. Wang, H.-S. Sheu, S.-H. Wu, B. J. Hwang, *Nano Energy* **2021**, *90*, 106542.

[66] Z. Zhang, J. Zhang, H. Jia, L. Peng, T. An, J. Xie, *J. Power Sources* **2020**, *450*, 227601.

[67] L. Peng, S. Chen, C. Yu, C. Wei, C. Liao, Z. Wu, H. L. Wang, S. Cheng, J. Xie, *ACS Appl. Mater. Interfaces* **2022**, *14*, 4179–4185.

[68] S. Shim, W. B. Park, J. Han, J. Lee, B. D. Lee, J. W. Lee, J. Y. Seo, S. J. R. Prabakar, S. C. Han, S. P. Singh, C. C. Hwang, D. Ahn, S. Han, K. Park, K. S. Sohn, M. Pyo, *Adv. Sci. (Weinh)* **2022**, *9*, e2201648.

[69] D. Spencer Jolly, Z. Ning, G. O. Hartley, B. Liu, D. L. R. Melvin, P. Adamson, J. Marrow, P. G. Bruce, *ACS Appl. Mater. Interfaces* **2021**, *13*, 22708–22716.

[70] Y. Zhu, X. He, Y. Mo, *ACS Appl. Mater. Interfaces* **2015**, *7*, 23685–23693.

[71] J. Auvergniot, A. Cassel, J. B. Ledeuil, V. Viallet, V. Seznec, R. Dedryvere, *Chem. Mater.* **2017**, *29*, 3883–3890.

[72] E. Gil-González, L. Ye, Y. Wang, Z. Shadike, Z. Xu, E. Hu, X. Li, *Energy Storage Mater.* **2022**, *45*, 484–493.

[73] G. Liu, W. Weng, Z. Zhang, L. Wu, J. Yang, X. Yao, *Nano Lett.* **2020**, *20*, 6660–6665.

[74] C. Zheng, J. Zhang, Y. Xia, H. Huang, Y. Gan, C. Liang, X. He, X. Tao, W. Zhang, *Small* **2021**, *17*, e2101326.

[75] J. Auvergniot, A. Cassel, D. Foix, V. Viallet, V. Seznec, R. Dedryvère, *Solid State Ionics* **2017**, *300*, 78–85.

[76] D. Zeng, J. Yao, L. Zhang, R. Xu, S. Wang, X. Yan, C. Yu, L. Wang, *Nat. Commun.* **2022**, *13*, 1909.

[77] L. Ye, X. Li, *Nature* **2021**, *593*, 218–222.

[78] L. Peng, H. Ren, J. Zhang, S. Chen, C. Yu, X. Miao, Z. Zhang, Z. He, M. Yu, L. Zhang, S. Cheng, J. Xie, *Energy Storage Mater.* **2021**, *43*, 53–61.

[79] S. Chen, C. Yu, S. Chen, L. Peng, C. Liao, C. Wei, Z. Wu, S. Cheng, J. Xie, *Chin. Chem. Lett.* **2022**, *33*, 4635–4639.

[80] S. Chen, C. Yu, C. Wei, L. Peng, S. Cheng, J. Xie, *Chin. Chem. Lett.* **2022**, doi: 10.1016/j.cclet.2022.05.058.

[81] S. Y. Kim, H. Cha, R. Kostecki, G. Chen, *ACS Energy Lett.* **2022**, *8*, 521–528.

[82] Y. Xia, J. Li, Z. Xiao, X. Zhou, J. Zhang, H. Huang, Y. Gan, X. He, W. Zhang, *ACS Appl. Mater. Interfaces* **2022**, *14*, 33361–33369.

[83] Z. Zhang, L. Wu, D. Zhou, W. Weng, X. Yao, *Nano Lett.* **2021**, *21*, 5233–5239.

[84] G. L. Zhu, C. Z. Zhao, H. J. Peng, H. Yuan, J. K. Hu, H. X. Nan, Y. Lu, X. Y. Liu, J. Q. Huang, C. He, J. Zhang, Q. Zhang, *Adv. Funct. Mater.* **2021**, *31*, 2101985.